CHAPTER 1

Ultrasound-Based Gas–Liquid Interface Detection in Gas–Liquid Two-Phase Flows

S. Roberto Gonzalez A*, Yuichi Murai and **Yasushi Takeda**

Contents

Abstract

Ultrasonic velocity profiler (UVP) measurements are performed for gas–liquid two-phase flow. The UVP measurements are conducted in a rectangular channel and in a pipe, both horizontally oriented. The liquid velocity measurements and ultrasound echo intensity

Division of Energy and Environmental Systems, School of Engineering, Hokkaido University, N13W8, Sapporo 060-8628, Japan

*Corresponding author: Currently at Nanyang Technological University, Division of Physics and Applied Physics, School of Physical and Mathematical Sciences, 21 Nanyang Link 05–13, Singapore 637371
E-mail address: sroberto@ntu.edu.sg

Advances in Chemical Engineering, Volume 37
ISSN: 0065-2377, DOI 10.1016/S0065-2377(09)03701-6

are used to locate the position of the gas–liquid interface information. Liquid velocity data are analyzed to obtain the bubble interface for the study of the mechanism of drag reduction. The peak ultrasound echo intensity is used to locate the position of the gas–liquid interface in a pipe for the estimation of the liquid flow rate. No gas-flow rate calculations are performed. The experiments in the pipe are performed using three UVP–DUO systems simultaneously to obtain a more accurate shape for the gas–liquid interface. The tests conducted belong to three different flow regimes: stratified, elongated bubble, and slug flow. The results show very good agreement with the actual liquid flow rates.

1. INTRODUCTION

The use of sound in science and technology can be traced back to as early as the 1950s. At that time, devices that used ultrasonic waves to detect flaws in metals were commercially available. The use of sound has spread to different fields such as medicine (Satomura, 1957; Wild and Reid, 1953), meteorology (Lhermitte, 1973), and oceanography (Pinkel, 1979). Takeda (1986) began to apply ultrasound to several problems of interest in fluid mechanics and heat transfer. The ability of an ultrasound-based technique that can provide velocity profile measurements in opaque flows gives it a crucial advantage over optical methods such as laser Doppler anemometry, particle tracking velocimetry, and particle image velocimetry (PIV). This was recognized by researchers who later applied ultrasound to other fluid-flow-related problems. Another field where the ultrasonic velocity profiler (UVP) has been well received is that of two-phase flows. Although originally developed to be used in single-phase flows, it can be applied to study multiphase flows, particularly gas–liquid flows. Zhou et al. (in Murakawa et al., 2003), Suzuki et al. (2002), and Murakawa et al. (2003, 2005) suggested a statistical approach to separate the velocity information of the gas and liquid phases. Gas–liquid two-phase flows are common in engineering and scientific applications; gas–liquid interface detection has been investigated using techniques such as hot-wire anemometry, laser Doppler velocimetry (Kitagawa et al., 2005), PIV (Suzuki et al., 2002), and imaging tomography (Murai et al., 2005, 2007). Ultrasound also can be applied in the detection of the gas–liquid interface. Wada et al. (2006) demonstrated the use of echo intensity for pattern recognition of two-phase flow. In this chapter, the detection of the gas–liquid interface is used to approach two different engineering problems that nowadays are the focus of extensive research. The first problem is the determination of the mechanism of bubble-based drag

reduction. The second problem is the detection of the gas–liquid interface for estimating the liquid flow rate of a gas–liquid two-phase flow. Ideally, we want to estimate both the gas- and liquid-phase flow rates, but current research has focused on the estimation of the liquid flow rate. Future research should lead to the accurate estimation of the gas-phase flow rate as well.

Recently, there have been papers published that report new ultrasound-based techniques for visualizing fluid flow. One technique is a high-frame-rate technique referred to as speckle correlation velocimetry. It was originally developed for imaging the propagation of low frequency shear waves in soft tissues (Sandrin et al., 1999). It was later used to obtain echographic images of a stretched vortex and a jet flowing through a hole 3 mm in diameter (Sandrin et al., 2001). To obtain local measurements of the flow, Manneville et al. (2001) proposed a technique based on the combination of classical ultrasonic Doppler velocimetry and two-dimensional echographic techniques. This appears to be an interesting method for extending the capability of ultrasonic Doppler velocimetry to two-dimensional local measurements and increasing the frame rates of normal scanners ($\sim$50–5,000 frames per second). Using two perpendicular transducer arrays, they mapped the flow of a stretched vortex.

This technique appears particularly attractive because the high frame rate allows the dynamics of fast changing liquid flows to be studied and the spatial resolution is significantly reduced using a high ultrasound frequency (Manneville et al., 2005). This technique can be adapted to small-scale, high-speed gas–liquid two-phase flows that are not presently subject to ultrasound-based techniques.

Section 2 describes the methodology for locating a gas–liquid interface. In this approach, only the liquid velocity is used to detect the interface. As previously mentioned, the motivation for developing this method is application to the investigation of the mechanism of bubble-based frictional drag reduction, which is the focus of a large research effort aimed at reducing the cost of transportation by ships. Using the idea suggested by Wada et al. (2006), Section 3 presents a method for detecting the gas–liquid interface by means of the peak ultrasound echo intensity. This method is used to estimate the liquid flow rate of gas–liquid two-phase flow in a horizontal pipe. Although the flow rate in a vertical configuration is more commonly measured (Oddie and Pearson, 2004), the flow rate of a two-phase mixture in a horizontal orientation is measured in the transport of oil–gas mixtures from wells to reservoirs (Cook and Behnia, 2000; Oddie and Pearson, 2004; Shemer, 2003) and in chemical and power generation processes. Therefore, a noninvasive device capable of accurately measuring the flow rate of the component phases in real time may be well received in these important engineering activities.

2. GAS–LIQUID INTERFACE INFERRED FROM LIQUID VELOCITY

The UVP system emits ultrasonic pulses along its measuring line. It provides velocity and echo intensity information for every profile captured. The accuracy of the measurements obtained using the UVP method are considered to be $\sim 3.5\%$ for velocity and $\sim 1.1\%$ for position under optimized conditions (Takeda, 1986). The overall experimental error expected in estimating the liquid flow rate is $\pm 5.1\%$; this value does not take into account the fact that the liquid flow is assumed to be one-dimensional in the calculation of the liquid flow rate. In liquid slugs and the volume of liquid below the bubbles, this appears to be a good approximation; however, in the regions near the leading edge and trailing edge of a bubble, the liquid flow is not one-dimensional. The principle of the UVP was described by Takeda (1986).

In this section, the UVP is applied to obtain the location of the gas–liquid interface of two-phase flow in a horizontal square channel. In this method, only the velocity data are used to obtain the position of the gas–liquid interface.

We propose signal processing of the UVP output. The gas–liquid interface is detected without using the echo intensity or any optical information. The method presented in this section represents an intermediate and necessary step in the development of an ultrasound-based sensor for reducing frictional drag. In the near future, a complete monitoring system for a bubbly two-phase boundary layer is to be developed. The system is to be applied to ships and pipelines.

2.1 Experimental setup

Figure 1 is a schematic diagram of the experimental setup. The test section is a horizontal rectangular channel 40 mm in height (H), 160 mm in width (W), and 6,000 mm in length (L). The rectangular channel is completely constructed of transparent acrylic resin, as shown in Figure 2. Tap water and air are used as the gas and liquid phases, respectively. Water is circulated by a 2.2 kW pump fed by a water reservoir 4.2 m away. Air bubbles are injected into the horizontal channel from the upper inner surface of the channel. An array of capillary needles produces bubbles 10–100 mm in length. Before the air and water are mixed, their volumetric flow rates are measured. After leaving the horizontal channel, the gas–liquid mixture is dumped into a tank that acts as a bubble remover; when the liquid phase is recirculated it is free of bubbles. At the end of the horizontal channel tracer particles are added to the water to act as ultrasound reflectors. The mean particle diameter is 200 μm and the particle density is $1020\,\mathrm{kg/m^3}$. These tracer particles are assumed to

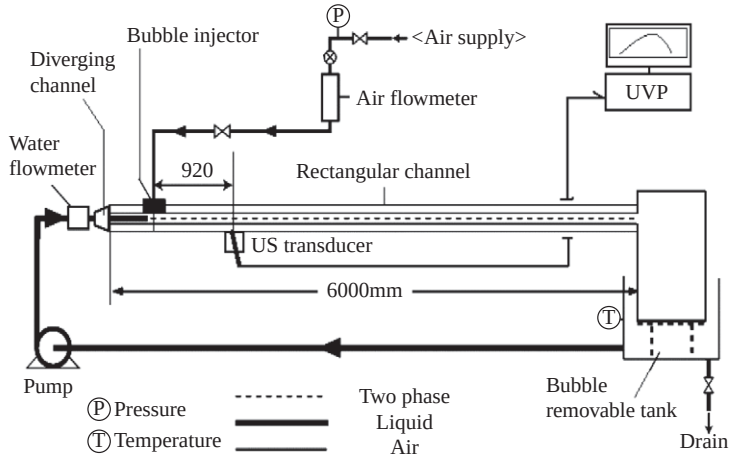

Figure 1 Schematic diagram of the experimental setup.

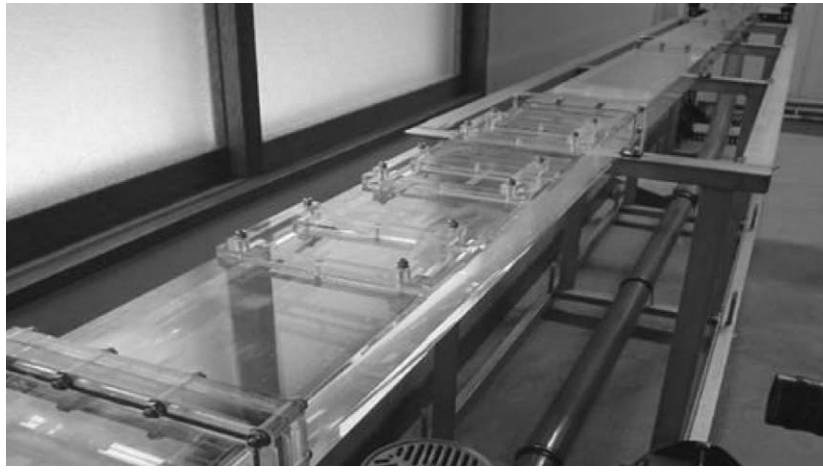

Figure 2 Horizontal channel for the gas–liquid two-phase flow experiments.

follow the liquid flow faithfully; this ability has been assessed by Melling (1997). The superficial velocity of the liquid varies from $V_l = 0.3\,\mathrm{m/s}$ to $1.5\,\mathrm{m/s}$; Reynolds number ranges from $\mathrm{Re}_H = 1.2 \times 10^4$ to $\mathrm{Re}_H = 6 \times 10^4$ on the basis of $\mathrm{Re}_H = V_l H/\nu$, where H is the channel height, V_l the superficial velocity of the liquid, and ν the kinematic viscosity of the liquid. The ultrasound transducer is 920 mm ($x/H = 23$) downstream of the injection point.

2.2 Experimental approach

Figure 3 shows three images taken from the top of the channel at $Re_H = 2.8 \times 10^4$. The size of the images is 160 mm × 160 mm. The flow direction is from left to right. α is defined as $\alpha = Q_g/(Q_a + Q_g)$, where Q_g is the gas-phase flow rate and Q_a the actual liquid-phase flow rate. In addition, the relative beam thickness is shown in the images. The maximum Weber number, We, is 10^3; $We = \rho V_l^2 d/\sigma$, where ρ is the liquid density, d the bubble diameter, and σ the surface tension of the liquid. Owing to the high value of We, individual bubbles are considerably deformed by the inertia of the fluid. In addition, images taken in the spanwise direction confirm (a) the translational velocity of the bubbles is lower than the mean velocity of the liquid and (b) all bubbles are confined to the upper part of the channel. Therefore, there is significant friction between the bubbles and the upper wall of the channel.

The gas–liquid interface is detected by taking advantage of the ultrasound behavior in the vicinity of the interface. At the gas–liquid interface, there is a large difference in acoustic impedance (density multiplied by the sound speed). Therefore, an ultrasound beam is mostly reflected at the gas–liquid interface. In addition, the ultrasound phase is reversed owing to the fixed pressure. The incoming ultrasound waves and those reflected at the interface create standing waves. The standing waves occur within a length of the pulsed ultrasound from the gas–liquid interface. Figure 4 is a schematic representation of the ultrasound beam reflected at the interface. The horizontal axis is the time evolution. Considering a four-cycle pulse as used in this study, four layers of weak pressure are created as a result of the standing waves. There are tracer particles in the regions where the standing waves occur; however, the echo scattered from the particles in these regions is rather weak. The particles that cross the standing waves produce two echoes; one is produced by the emitted wave and one is produced by the receding wave. The net result is that no net Doppler shift is produced although component shifts exist. Consequently, the output of the UVP system

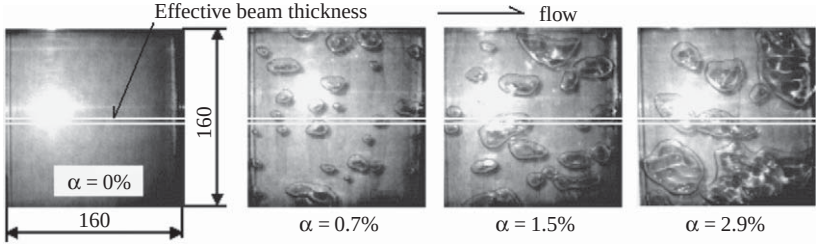

Figure 3 Bubble size for different α values compared with the effective thickness of the ultrasound beam.

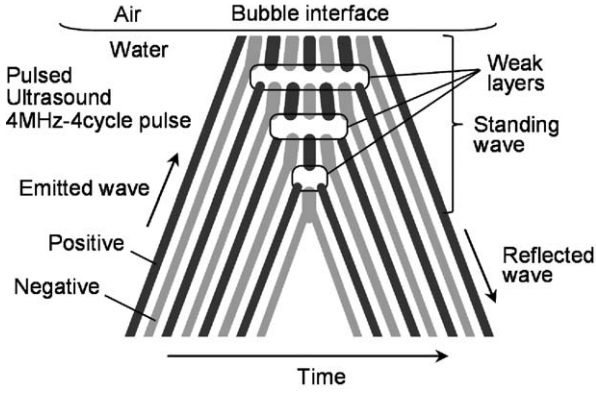

Figure 4 Reflected four-pulse ultrasound wave at the gas–liquid interface.

(UVP–DUO, Met-Flow Inc.) is near zero velocity in this region. This phenomenon can be exploited to detect the position of the gas–liquid interface. The thickness of the standing wave perpendicular to the interface can be estimated by

$$\varphi = \frac{1}{2}\lambda N_{UC} \cos\theta \tag{1}$$

where λ is the ultrasound wavelength, φ the thickness of the standing wave, N_{UC} the number of cycles per ultrasonic pulse, and θ the inclination angle with respect to the flow. The estimated standing wave thickness is 0.74 mm for a 4 MHz four-cycle pulse ultrasound system.

As previously mentioned, the UVP–DUO system outputs near zero velocity in the vicinity of the gas–liquid interface. Therefore, large velocity gradients exist in this region. In image processing, several methods have been proposed to detect changes in pixel intensity and perform pattern recognition. Such an approach is used here. A linear filter is applied to the velocity values to detect rapid changes in the velocity near the gas–liquid interface. The filters applied are 3×3 square regions centered at every point (i,j) as shown in Figure 5 (Yang, 1994). Figure 6a shows the raw velocity data obtained by the UVP. In the upper part of the image, the gas phase is present but not visible. The ultrasound transducer is placed at the bottom of the acrylic channel in a water jacket. Multiple reflections occur at $y/H \sim 0.5$ and a horizontal line (the original liquid-phase velocity values) is observed in Figure 5a. This line is magnified in Figures 6b and c, after applying the Laplacian and first-order spatial differentiation filters, respectively; however, this line is outside the region of interest of the gas–liquid interface. Figure 6b shows the resulting image after the Laplacian filter is applied to the velocity values; this filter enhances intensity variations. In the upper part of the

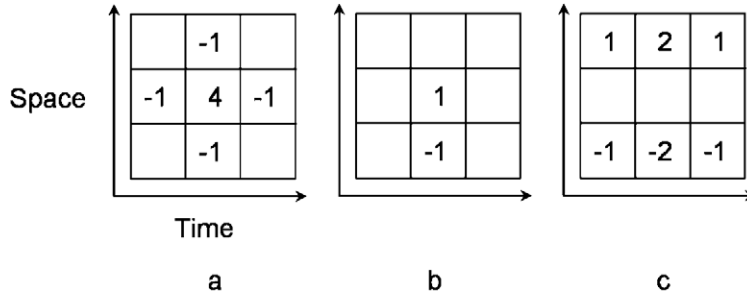

Figure 5 Filters applied to the UVP velocity values: (a) Laplacian, (b) forward differentiation, and (c) Sobel.

image, the regions of light color indicate possible locations where the gas–liquid interface may be located; however, this region does not provide a good contrast for extracting the bubbles present in the image. Figure 6c shows the results for the first-order spatial differentiation filter. Unfortunately, this filter is not able to accurately determine the location of the interface. The upper part of the pipe, which is occupied by the gas phase, appears to be occupied by a continuous medium; this is not so, the gas phase consists of discrete bubbles separated by short liquid slugs. Consequently, it is not possible to apply a threshold to the image because (a) the contour of the gas phase cannot be accurately obtained and (b) too much liquid-phase information is discarded. Figure 6d shows the results of applying a Sobel filter and threshold level. This filter appears to work best in detecting spatial changes. The gas phase can be seen in the upper part of the pipe. After the filter is applied, the image is binarized. Each column of pixels is examined; pixels on and above the gas–liquid interface are given the value 1; pixels below the gas–liquid interface are given the value zero. Figure 6e shows the resulting Sobel image after binarization. This image displays more clearly the location and number of bubbles present in the liquid flow. Finally, Figure 6f shows the two-phase flow image with the gas phase highlighted in the upper part of the pipe. In this image, only the liquid velocity and gas–liquid interface are available; the translational velocity of the bubbles present in the flow is not obtained. In summary, the Sobel filter provides the most accurate representation of the distribution of the bubbles in the flow.

It is worth mentioning that there are two necessary conditions for this method to be applied successfully. One is that there must be enough particles to act as ultrasound reflectors along the measurement line, or else the near zero velocities near the interface are not detected. The second is that the wavelength of the gas–liquid interface shape must be larger than $\sim 10\lambda$. Therefore, the leading and trailing edges of individual bubbles cannot be detected owing to their strong curvature. Small solid

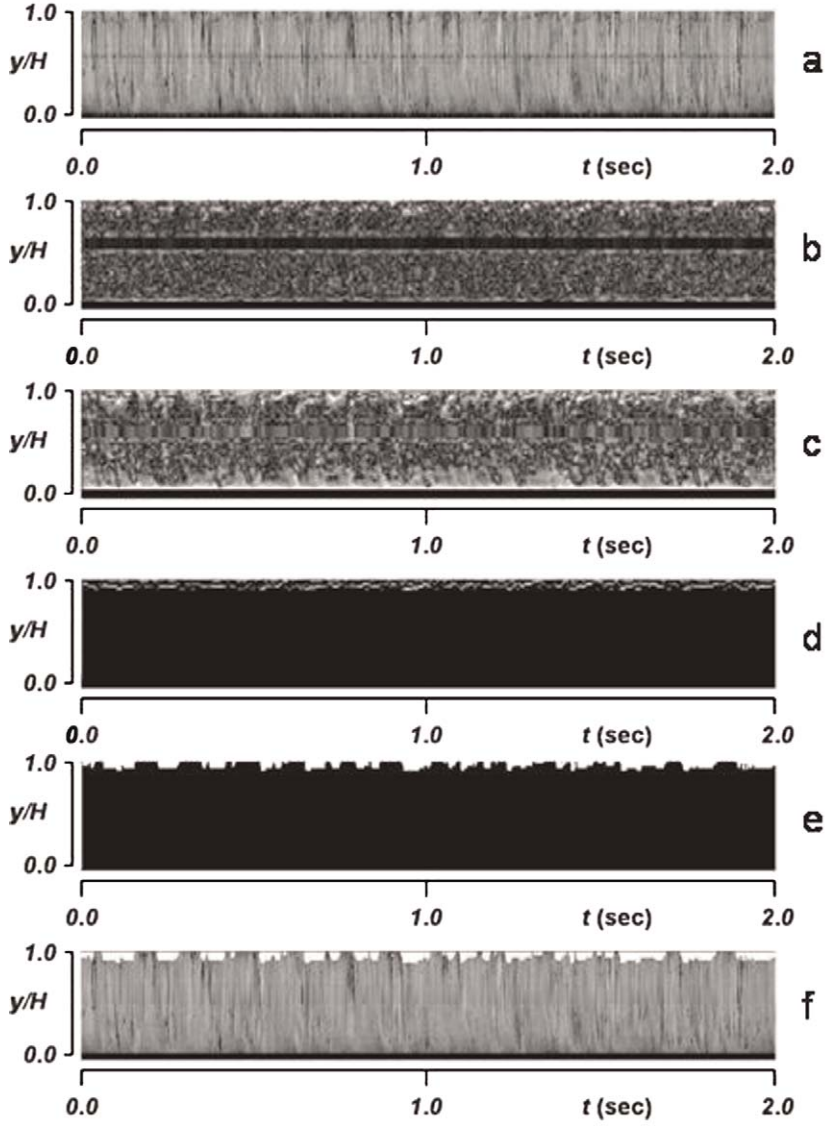

Figure 6 UVP data: (a) raw velocity data, (b) data using a Laplacian filter, (c) data using a forward differentiation filter, (d) data using a Sobel filter, (e) binarized Sobel data, and (f) gas-phase detected after the application of the Sobel filter.

particles can act as ultrasound scatterers since they reflect enough of the ultrasound energy back to the transducer; however, the leading and trailing edges of large bubbles (much larger than the solid particles) do not reflect the ultrasound beam strongly enough to the transducer.

Consequently, it is more difficult to detect the gas–liquid interface accurately in the vicinity of the leading and trailing edge of the bubbles.

2.3 Validation of the proposed experimental method

Figure 7a shows an example of the applicability of the method described; the horizontal axis only shows the first 500 ms of the UVP data acquired so that detail of the shapes of bubbles (black) at the top of the channel can be seen. Figure 7b is a qualitative image of the liquid velocity distribution. Low velocities are indicated by blue and high velocities by green. The velocities in this image are subtracted from the mean liquid velocity of each velocity profile. Figure 7c shows the velocity gradients along the height of the channel, du/dy. As in Figure 7b, blue indicates low du/dy values and green high du/dy values. Once the gas–liquid interface is detected, various studies can be performed. The relevance of this method is that it allows the detection of the gas–liquid interface without the need to have ultrasound echo intensity information. However, this method is best suited for flows where the void fraction is low (i.e., up to

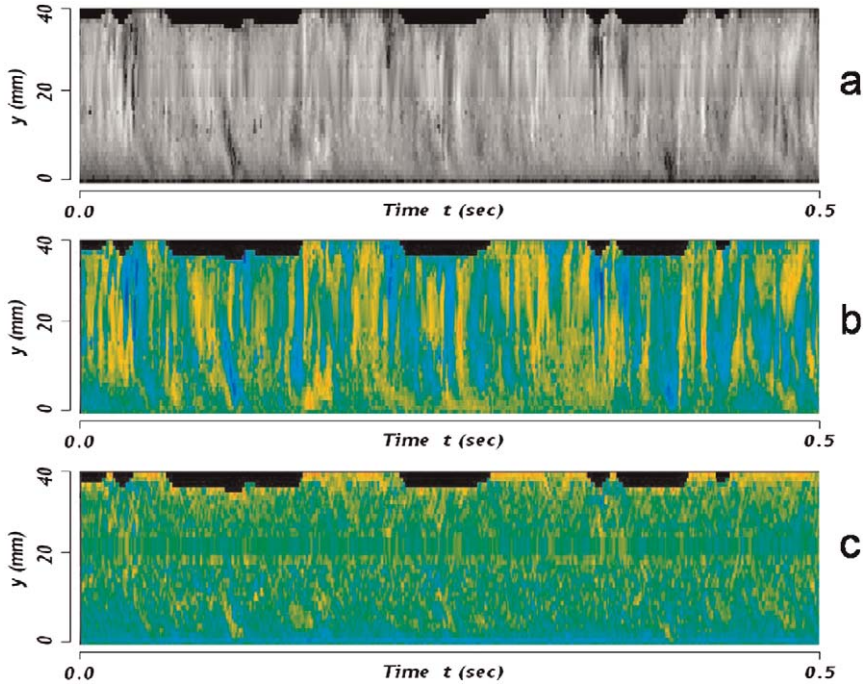

Figure 7 UVP data: (a) gas−liquid interface detected, (b) u distribution (subtracted from mean liquid velocity of each velocity profile), and (c) du/dy profile.

10%). In many engineering applications, gas–liquid flows of larger gas void fractions are encountered. In the next section, a method is described that makes use of the peak ultrasound echo intensity to detect the location of the gas–liquid interface in such flows.

3. GAS–LIQUID INTERFACE INFERRED FROM THE PEAK ULTRASOUND ECHO INTENSITY

In this section, the peak ultrasound echo intensity is used to locate the position of the gas–liquid interface flowing in a horizontal pipe. The accurate detection of the gas–liquid interface in pipe flow has important implications in engineering.

(a) The gas–liquid interface is an important parameter for predicting the behavior of these types of two-phase flows. Suggested models for predicting the unsteady behavior of two-phase flows (Duckler and Hubbard, 1975; Fossa et al., 2003; Taitel and Barnea, 1990) require the average length of the slugs to characterize the flow. Accurate gas–liquid interface detection may lead to better models for predicting two-phase flows. Moreover, two-phase flow process equipment can be improved if the statistical expected values of the liquid slug length are available to design engineers. Not only more reliable but also more efficient equipment can be developed.

(b) The position of the gas–liquid interface can be used to determine the portion of the cross-sectional area of the pipe occupied by the liquid phase; the liquid flow rate can be estimated from the liquid phase velocity distribution and area occupied. This may lead to the development of a flow metering device that can be applied in a gas–liquid two-phase flow.

In gas–liquid two-phase flow, several flow patterns exist such as bubbly, slug, plug, and annular flow depending on the pipe configuration, geometry, and flow conditions. Of these types of flows, slug flow is one of the most complex, owing to its intermittent and transient nature. Despite its complexity, industrial processes often require an online, accurate, and noninvasive estimation of such flow. If this is accomplished, industrial processes can be kept within acceptable quality limits and additionally, financial losses may be reduced.

With regard to multiphase flow measurement, two of the most commonly used flow meter devices in industry are the Coriolis flow meter and electromagnetic flow meter. The Coriolis flow meter is widely used owing to its high accuracy (Tavoularis, 2005) but it assumes (a) the phases do not slip with respect to each other when oscillated and (b) the phases are not compressible (Oddie and Pearson, 2004). Therefore,

the device is suitable in solid–liquid and liquid–liquid flow applications, but it may not be acceptable in solid–gas or gas–liquid application.

On the other hand, electromagnetic flow meters process signals that depend on the electromagnetic conductivity of the phase of the flow. Cha et al. (2002) reported good results using an electromagnetic flow meter designed by their research team. However, they noticed a decrease in accuracy between experimental and theoretical values as the void fraction increased. This two-phase flow metering method appears attractive. It is nonintrusive and has no moving parts and is therefore maintenance free, but it may require a separate measurement of the density for the mass flow rate measurements (Oddie and Pearson, 2004). Approaching the gas–liquid flow metering problem by means of the use of ultrasound is advantageous. It is also a nonintrusive method and has no moving parts. In addition, the mass flow rate can be measured by adding a temperature sensor to the system and correlating the temperature to a density value to obtain the corresponding mass flow rate.

3.1 Experimental setup

The experimental setup can be seen in Figure 8. It mainly consists of the gas–liquid two-phase flow loop and three UVP–DUO systems. The pipe loop is made of plexiglass and has an inner diameter D of 40 mm. It consists of a water reservoir, a water pump controlled by a frequency inverter, liquid- and gas-phase flow meters, a pneumatic valve, and the

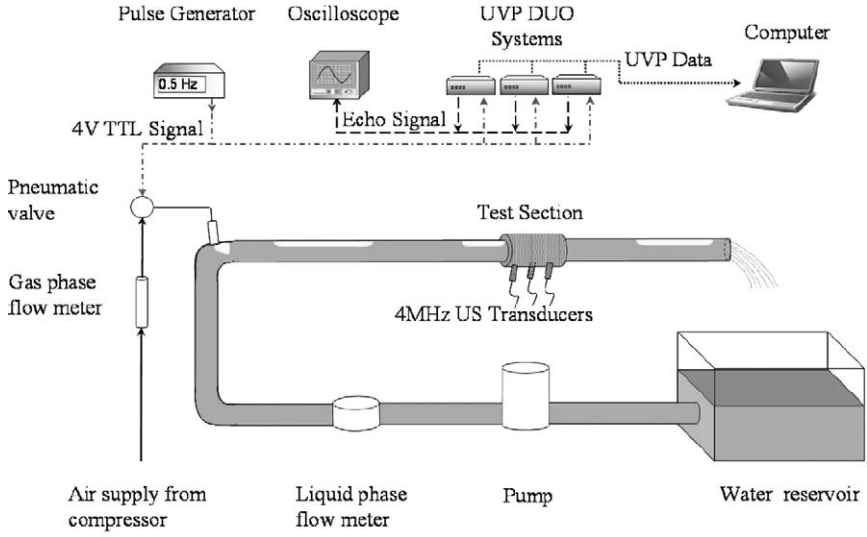

Figure 8 Experimental setup.

test section for the UVP measurements. For the UVP measurements, the three UVP–DUO systems, a pulse generator, an oscilloscope, and a personal computer are used. Water and air are used as the liquid and gas phases, respectively. The water is fed into the pump from the water reservoir. The liquid-phase flow meter is installed 1.4 m downstream of the pump. The water flows through the pipe loop and returns in a horizontal path. The gas phase is added at the beginning of the horizontal path. Before the gas is added to the liquid phase, its volumetric flow rate is measured. In this way, the desired void fraction for each test is set. The test section housing the three ultrasonic transducers is located $60D$ from the entrance of the gas phase. It is a cylinder with an inner diameter of 40 mm and length of 90 mm made of a material that absorbs ultrasonic sound. The absorbent material of the test section is selected to avoid interference among the UVP transducers due to their proximity to each other. A schematic diagram of the test section can be seen in Figures 2a and b.

The transmitting frequency f of the UVP−DUO systems is 4 MHz in all tests. The ultrasound wavelength λ is 370 μm and the sound velocity in water c is 1,480 m/s. 100 mm ion exchange (Diaion) particles are added to the flow as flow tracers; their ability to follow the liquid flow has been assessed using Basset's analysis (Melling, 1997). Owing to theoretical considerations, the size of the flow tracers must be larger than one quarter of the emitted ultrasonic burst (Met-Flow, 2002).

Each test begins when a 4 V transistor–transistor logic signal from the pulse generator triggers the three UVP–DUO systems and pneumatic valve; the pneumatic valve allows the entrance of the gas phase into the pipe loop and this creates the bubbles that are added to the liquid phase. The frequency of the signal from the pulse generator is 0.5 Hz in all tests. When the tests are conducted, both the gas flow rate and the liquid flow rate are set to the desired values. The actual liquid flow rate Q_a is measured by collecting water in a bucket for a certain period. The UVP measurement is performed and the estimated liquid flow rate Q_e is compared against the actual liquid flow rate.

Re_D based on the superficial velocity of the liquid V_l and pipe diameter D ranged from 5.3×10^3 to 6.4×10^4. V_l ranged from 0.13 m/s to 1.6 m/s. Re_D is defined as $\mathrm{Re}_D = V_l D/\nu$, where ν is the kinematic viscosity of the liquid. The superficial gas velocity V_g ranged from 0.01 m/s to 0.7 m/s.

3.2 Experimental method

For each UVP file created, one gas–liquid interface height time series $h_n(N)$ is obtained; $n = 1,2,3$ (one time series for each transducer) and N is the velocity or ultrasound echo intensity profile number. The gas–liquid

interface height is obtained as follows. Each UVP file contains velocity and echo intensity information. From each echo intensity profile, the position of the maximum absolute echo intensity is located and labeled as the location where the gas–liquid interface is found; that is

$$h_n(N) = Max\left|E_I(k)\right|, \quad 0 \le k \le k_{\max} \tag{2}$$

where $h_n(N)$ is the gas–liquid interface location, $E_I(k)$ the raw ultrasound echo intensity, k the channel number, and $k_{\max}$ the closest channel to the upper wall of the pipe. The ultrasound echo intensity values are then binarized; above the channel of maximum ultrasound echo intensity, the gas–liquid interface, the intensity is set to zero; at the channel of maximum ultrasound echo intensity and below the intensity is set to 1. This process is done for each of the three UVP files created in each flow condition; therefore, three gas–liquid interface height time series are obtained. Although their data acquisitions begin simultaneously, each ultrasonic transducer detects the gas–liquid interface at a different time; this is due to their positions in the test section (Figure 9a). The gas–liquid interface is first detected by transducer 2 (connected to UVP–DUO system 2), then transducer 1 and finally transducer 3.

It is desirable to consider the interface heights of the three transducers with transducers 1 and 3 being to the left and to the right of transducer 2, respectively, as shown in Figure 9b. When only one transducer is used, the gas–liquid interface is assumed to be flat as in Figure 10a (line p–p'); then the area occupied by the liquid phase near the wall of the pipe and above the gas–liquid interface is ignored. With three transducers, however, a more accurate gas–liquid free surface shape may be obtained

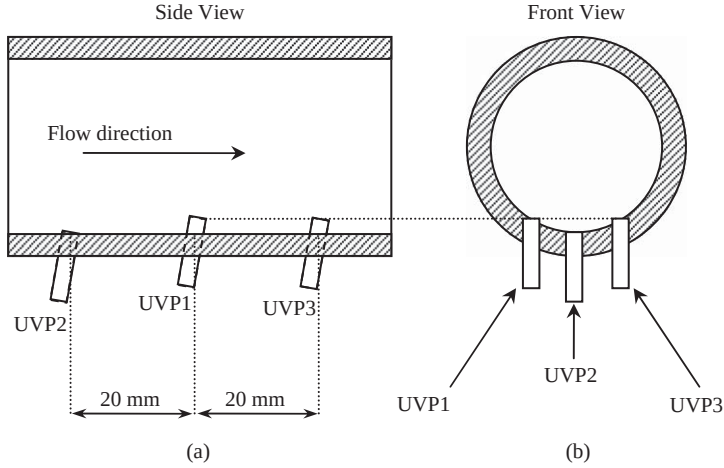

Figure 9 Ultrasound transducer arrangement in the test section: (a) side view and (b) front view.

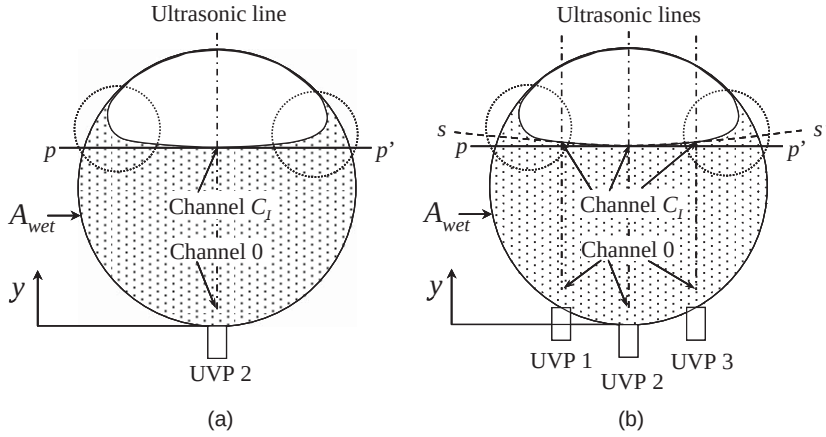

Figure 10 (a) One transducer and (b) three transducers.

(line *s*–*s*′ in Figure 10b. With three points of the gas–liquid interface, the area ignored in the calculation of A_{wet} is reduced.

3.2.1 Correlation analysis

A correlation analysis is performed to align the positions of the gas–liquid interface detected by the UVP transducers as if they are located on the same *x*–*y* plane. As mentioned earlier, the gas–liquid interface height series from the UVP transducers 1, 2, and 3 are $h_1(N)$, $h_2(N)$, and $h_3(N)$, respectively. Each series consists of 4,096 elements ($N_{\max}$), i.e., the number of velocity/ultrasound echo intensity profiles captured, $N = 0,1, \ldots, 4,095$.

The correlation coefficient is defined as

$$C_c(i) = \frac{\sigma_{j,k}}{\sigma_j \sigma_k} \tag{3}$$

where $\sigma_{j,k}$ is the covariance of the gas–liquid interface height for series j and k, σ_j the standard deviation of the gas–liquid interface height for series j (transducer 2) where series j consists of N–i elements and $j = 2$, and σ_k the standard deviation of the gas–liquid interface height for series k (transducers 1 and 3) where series k consists of N–i elements and $k = 1$, 3 and $0 \leq i \leq 10$.

As mentioned in Section 3.2, owing to the position of the UVP transducers along the pipe, the gas–liquid interface height is determined first by transducer 2, then transducer 1 and finally transducer 3. The positions of the gas–liquid interface heights determined by the transducers are similar but differ slightly. The value of i in Equation (3) that maximizes the correlation coefficient between series 2 and 1 is denoted i_{2-1} and the value that maximizes the correlation coefficient between

series 2 and 3 is denoted i_{2-3}. Once i_{2-1} and i_{2-3} are found, the series can be aligned. The maximum of the two values determines the final length of the series. Once the interface height series are aligned and resized, they consist of the following elements:

$$h_1(N) \quad i_{2-1} \leq N \leq N_{\max} - (i_{2-3} - i_{2-1}) \tag{4a}$$

$$h_2(N) \quad 0 \leq N \leq N_{\max} - i_{2-3} \tag{4b}$$

$$h_3(N) \quad i_{2-3} \leq N \leq N_{\max} \tag{4c}$$

Not only do the series have the same number of elements but also the gas–liquid interface heights of the series appear as if the three transducers are located in the x–y plane where transducer 2 is originally located. The next step determines the curvature of the interface from these three points.

3.2.2 Calculation of the portion of the pipe occupied by the liquid phase A_{wet}

We consider a square area as shown in Figure 11. This area is divided into 40,000 square elements. When summing the areas of the square elements in the circle in Figure 11a, the value obtained differs from the circular area by 0.1%. The locations of transducers 1, 2, and 3 and the locations of the gas–liquid interface heights are x_1, x_2, and x_3 and $s_1(x_1,y_1)$, $s_2(x_2,y_2)$, and $s_3(x_3,y_3)$, respectively. In the range $x_1 \leq x \leq x_3$, the free surface is calculated by a cubic polynomial function (spline interpolation), as shown by Kreyszig (1999). In the ranges $0 \leq x \leq x_1$ and $x_3 \leq x \leq x_f$, the gas–liquid interface is calculated by a linear extrapolation. The slope of

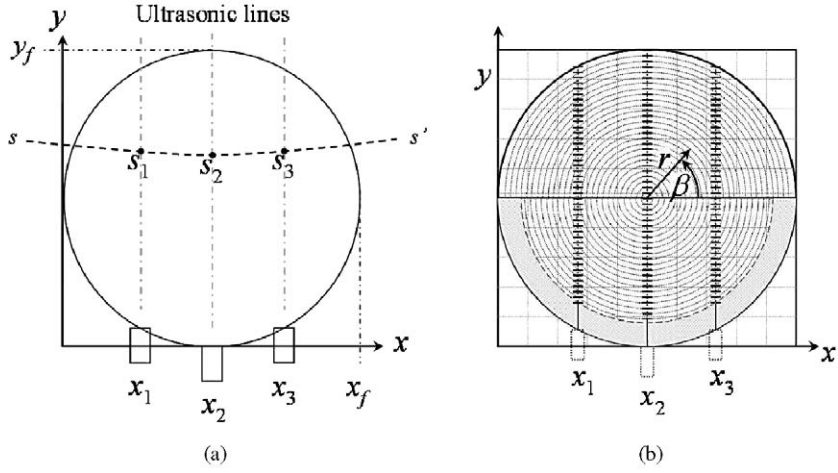

Figure 11 (a) Gas–liquid interface height position and (b) channel distribution.

the height in these ranges is the slope of the curve at x_1 and x_3, respectively.

Next, the values inside the circular area are binarized. The values above the gas–liquid interface are set to zero. The values below and those of the gas–liquid interface are set to 1. Summing all areas of the square elements of value 1, the portion of the pipe occupied by the liquid phase A_{wet} is obtained.

The velocity values obtained from the three UVP transducers are distributed along the vertical lines of $x = x_1$, $x = x_2$, and $x = x_3$, as shown in Figure 11b. Next, the velocity values are distributed radially. The cross-sectional area of the pipe is considered to be composed of three areas: the upper part of the pipe (above the middle of the pipe), the lower part of the pipe (from the first measurement to the channel closest the middle of the pipe), and the bottom region of the pipe, the region below the location of the first measurement (the gray shaded region). If the gas–liquid interface is above the middle of the pipe then the velocity values (from transducers 1 and 3) above the middle of the pipe and the same number of channels below the middle of the pipe are averaged. If the gas–liquid interface is below the middle of the pipe then the velocity values from transducers 1 and 3 are averaged. With regard to the transducer 2 values, if the gas–liquid interface is above the middle of the pipe then the values above the middle of the pipe and the same number of channels below the middle of the pipe are averaged. If the gas–liquid interface height is below the middle of the pipe then the transducer 2 values are simply distributed radially. It can be seen from Figure 11b that some overlap takes place; however, the number of channels from transducers 1 and 3 that overlap with those of transducer 2 is no more than 25%.

At the bottom of the pipe, the gray shaded region, the following liquid velocity values apply:

$$\text{For } 180 \leq \theta < 250, \quad V(r,\theta) = 0.7\overline{V}_{\text{UVP1}} \tag{5a}$$

$$\text{For } 250 \leq \theta < 290, \quad V(r,\theta) = 0.7\overline{V}_{\text{UVP2}} \tag{5b}$$

$$\text{For } 290 \leq \theta \leq 360, \quad V(r,\theta) = 0.7\overline{V}_{\text{UVP3}} \tag{5c}$$

$\overline{V}_{\text{UVP1}}$, $\overline{V}_{\text{UVP2}}$, and $\overline{V}_{\text{UVP3}}$ are the average liquid velocities for transducers 1, 2, and 3, respectively, from channel 0 to the channel where the gas–liquid interface is located. The constant 0.7 is obtained in the region $0 \leq y < 3.6$ from the power law equation (Munson et al., 1990). This equation is used in single-phase turbulent flow; the assumption made here is that the gas phase is located in the upper part of the pipe and the liquid velocity, not disturbed by the gas phase, develops in the lower part of the pipe as it does in single-phase turbulent flow.

The positions of the velocity values, so far distributed in cylindrical coordinates, are converted to Cartesian coordinates. The liquid flow rate is estimated by multiplying each velocity value $V(x,y)$ with its corresponding binary element $B(x,y)$.

$$Q_e = \frac{\sum_{t=t_i}^{t=t_f} \sum_{x=0}^{x=x_f} \sum_{y=0}^{y=y_f} V(x,y) \cdot B(x,y) \cdot t}{\sum_{t=t_i}^{t=t_f} t} \tag{6}$$

In the liquid flow rate calculation, one-dimensional flow is assumed; however, it is acknowledged this is not true in the vicinity of the bubbles (especially at their leading and trailing edges) where the relative velocity between the bubbles and the liquid phase creates a complex liquid motion that is far from one dimensional.

3.3 Validation of the experimental approach

The experimental approach described earlier is validated by performing experiments at different liquid flow rates and void fractions. The liquid flow rates tested are 0.6, 1.8, 2.8, 3.4, 4.5, 5.2, 6.2, and 7.5 m^3/h. The void fraction α in the experiments is 0% (liquid phase only), 10%, 20%, 30%, 40%, and 50%. Here again the void fraction α is defined as

$$\alpha = \frac{Q_g}{Q_a + Q_g} \tag{7}$$

where Q_g is the gas-phase flow rate and Q_a is the actual liquid-phase flow rate. The difference between the actual liquid flow rate Q_a and the estimated liquid flow rate Q_e is expressed by

$$\delta_e = \frac{Q_e - Q_a}{Q_a} \tag{8}$$

The sample rate of the experiments ranged between 8 and 12 ms. The flow rates of the gas phase and liquid phase are set to desired values before each test is performed and then the flow rate is measured by pouring the mixture into a bucket for a certain period. The volumetric flow rate of the liquid phase is then calculated and recorded; this is the actual flow rate Q_a. Next, the UVP measurements are performed.

Figure 12 shows the estimated liquid flow rate versus the actual liquid flow rate. The tests for $Q_a = 0.6\,m^3/h$ are of the stratified flow type. The tests of $1.8 \leq Q_a \leq 7.5\,m^3/h$ are of the elongated bubble and slug flow type (Brennen, 2005; Govier and Aziz, 1972). In this study, the flow conditions are compared with the flow regime charts of Govier and Omer (1962 in Govier and Aziz, 1972) and Mendhane (1974 in Brennen, 2005).

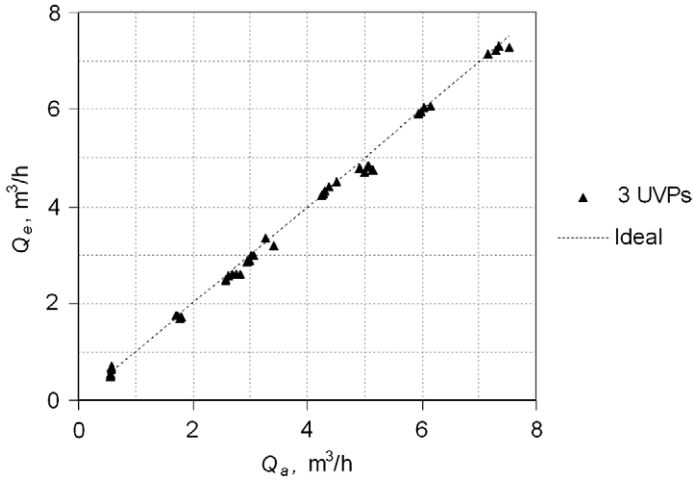

Figure 12 Q_a vs Q_e.

The chart of Mendhane contains flow regime boundaries for several pipe diameters, i.e., 25, 30, and 50 mm (horizontally oriented). The inner diameter of the pipe used in this study is 40 mm; therefore, the chart can be used as a reference to compare against. However, the chart does not indicate a boundary between the elongated bubble and slug flow regimes. The chart by Govier and Omer, although it is for air–water mixtures flowing in a 26 mm inner diameter horizontal tube does indicate a border between the elongated and slug flow regimes. It is acknowledged that the boundaries of the flow regimes are empirical transition lines and may vary slightly for a 40 mm inner diameter pipe, but as previously mentioned, the cited charts are used as references to describe the type of flow visualized by the UVP.

Figure 12 shows a good comparison between the estimated and actual liquid flow rates in the range tested although in some tests, i.e., those of $Q_a = 5\,\text{m}^3/\text{h}$ and $Q_a = 7.5\,\text{m}^3/\text{h}$, there is a slight underestimation. However, this graph does not show clearly how the different void fractions tested affect the ability of the method to estimate the liquid flow rate. Figure 13 is a surface plot of δ_e under each flow condition (Q_a and α). Although the graph shows a wide δ_e range, −10 to 20%, this is due to the tests of $Q_a = 0.6\,\text{m}^3/\text{h}$ where some values for δ_e are larger than in other tests. The experiments conducted in the range $1.8 \leq Q_a \leq 7.5\ \text{m}^3/\text{h}$ have a narrower range; in this range, the largest value for δ_e of 1.9% is at $Q_a = 1.8\ \text{m}^3/\text{h}$ and $\alpha = 50\%$ and the lowest value for δ_e of –8.2% is at $Q_a = 2.8\ \text{m}^3/\text{h}$ and $\alpha = 0\%$. From normal distribution relations, the 95% confidence interval for δ_e is

$$R_e = \mu_{\delta_e} \pm 2\sigma_{\delta_e} \tag{9}$$

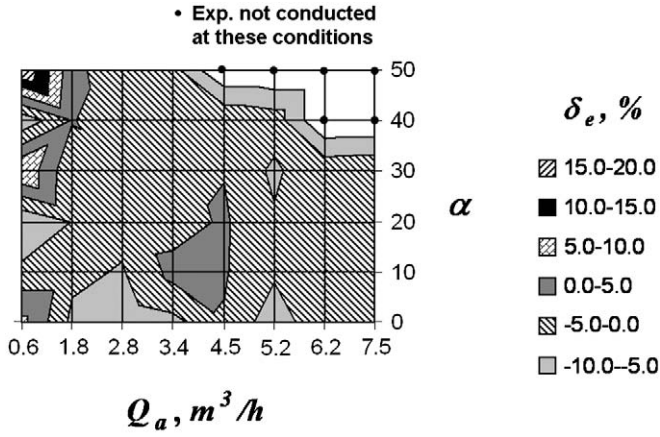

Figure 13 δ_e at different α values.

where R_e is the 95% confidence interval of the δ_e values, μ_{δ_e} the average of the δ_e values, and σ_{δ_e} the standard deviation of the δ_e values.

From Equation (9), $R_e = -1.9 \pm 2 * 5.1\%$ in the range $0.6 \leq Q_a \leq 7.5\, m^3/h$. This may be not suitable for an industrial or scientific application. However, in the range $1.8 \leq Q_a \leq 7.5\, m^3/h$, the 95% confidence interval is $R_e = -2.6 \pm 2 * 2.6\%$. Although the absolute average of the tests performed increases, more importantly, the standard deviation of these tests decreases by 42%.

Figures 14–16 show results of selected tests. These tests are selected because they are for three different flow regimes (Govier and Aziz, 1972). Figure 14 shows the test for $Q_a = 0.6\,\mathrm{m}^3/\mathrm{h}$ and $\alpha = 0\%$; the superficial liquid velocity is $V_l = 0.13\,\mathrm{m/s}$ and the intensity graphs, Figures 14a and b, show the first 1,000 velocity profiles (or 24%) of the 4,096 profiles captured. If all velocity profiles are displayed, important details of the flow may be lost. The color scale is the liquid velocity, the x-axis is the velocity profile number, and the y-axis is the pipe transverse distance. This test is of the stratified flow regime, and thus it is known that the liquid phase does not fill the entire cross-sectional area of the pipe; however, this is not clear from Figure 14a. After the ultrasound echo intensity is processed and the maximum ultrasound echo intensity of each velocity profile is detected, the gas–liquid interface is easily observed. The gas–liquid interface is located at $y = 25\,\mathrm{mm}$, as shown in Figure 14b. Both Figures 14a and b show the same velocity information, but Figure 14b shows the velocities after the gas–liquid interface has been detected; the interface height shown in this figure corresponds to that obtained by transducer 2, the transducer at the bottom of the pipe; the flat, quasi uniform interface clearly seen in the velocity profiles along the horizontal axis is shown in Figure 14b. There are a few velocity profiles for which the gas–liquid interface was not

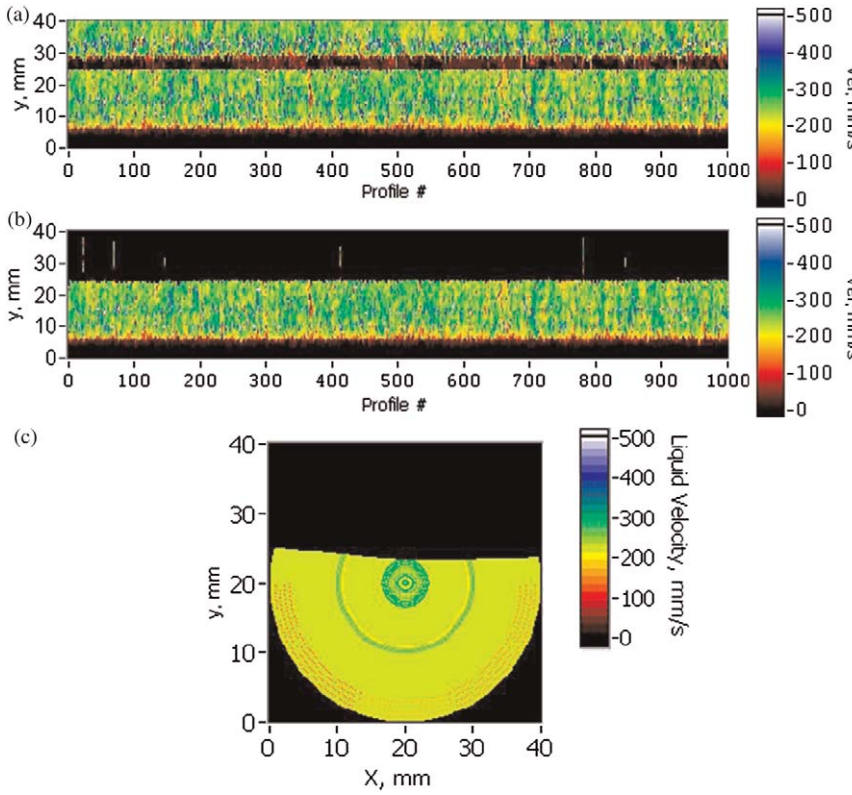

Figure 14 $Q_a = 0.6\,m^3/h$, $\alpha = 0\%$: (a) raw velocity values, (b) liquid velocity values after gas—liquid interface is detected, and (c) flow map, velocity profile # 50 (see Plate 1 in Color Plate Section at the end of this book).

accurately detected, but they form a low percentage ($< 1\%$) of the velocity profiles displayed. There are no liquid velocity values for $0 \leq y \leq 3.6\,mm$; the first UVP measurement is taken 3.6 mm from the bottom of the pipe. Figure 14c shows a flow map (velocity profile #50) of the cross-sectional area of the pipe. The gas–liquid interface heights detected by the three transducers are very similar; the interface is not flat as expected but instead shows a very small curvature. The velocity of the liquid is higher near the center of the pipe. The lighter (yellow) lines in the lower part of the pipe and near the wall correspond to values of the liquid velocity obtained from the power law equation (Equations 5a–c).

Figure 15a shows the raw data of the test of $Q_a = 1.8\,m^3/h$ and $\alpha = 10\%$; the superficial liquid and gas velocities are 0.4 and 0.04 m/s, respectively. This flow condition is in the elongated flow regime (Brennen, 2005; Govier and Aziz, 1972). Even though the flow is turbulent, the turbulence in the flow is not sufficiently large to overcome the rising drift

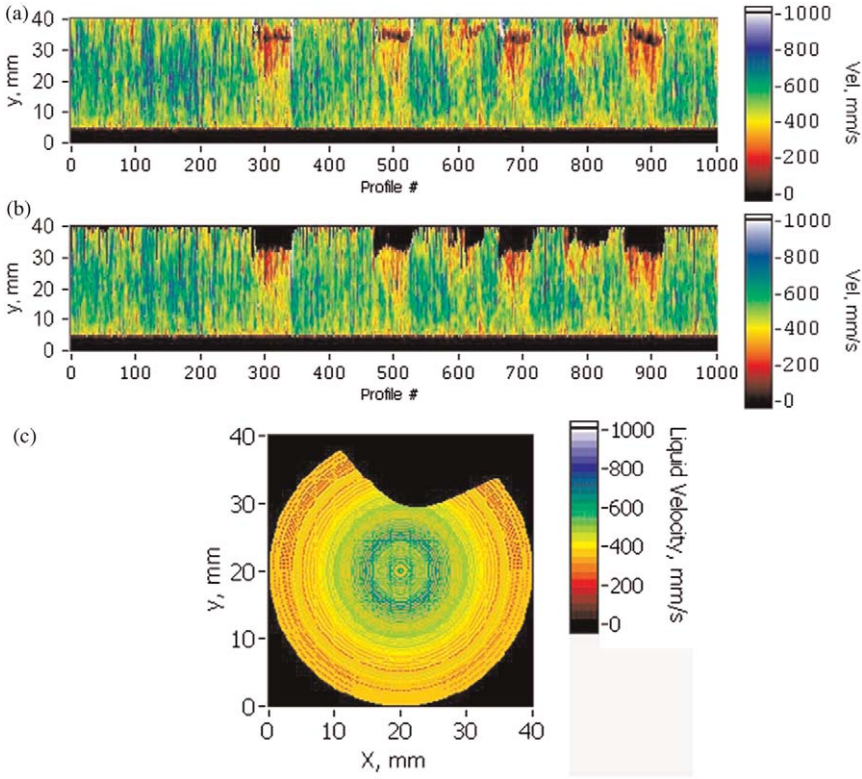

Figure 15 $Q_a = 1.8\,m^3/h$, $\alpha = 10\%$: (a) raw velocity values, (b) liquid velocity values after gas–liquid interface is detected, and (c) flow map, velocity profile # 495 (see Plate 2 in Color Plate Section at the end of this book).

of the bubbles due to the high-density ratio. Therefore, long bubbles located at the upper wall of the pipe are expected. Figure 16b shows the bubbles present in the flow (black regions in the upper part of the pipe) after the UVP data are processed. The first ~ 280 velocity profiles correspond to the liquid phase only, and then bubbles can be seen at periodic intervals. All bubbles are elongated and located in the region $29 \leq y \leq 40\,mm$. In addition, it is to be noted that the liquid slugs (lighter colored regions) move faster than the liquid layer below the bubbles. These elongated bubbles are analogous to the Taylor bubbles observed in vertical flow. Figure 15c shows the cross-sectional area of the pipe. Velocity profile #495 is shown. This liquid velocity profile belongs to the liquid below the middle section of the second bubble. It shows that the gas phase is not symmetrically distributed at the top of the pipe. In addition, the liquid velocity is higher at the center of the pipe and tends to decrease radially.

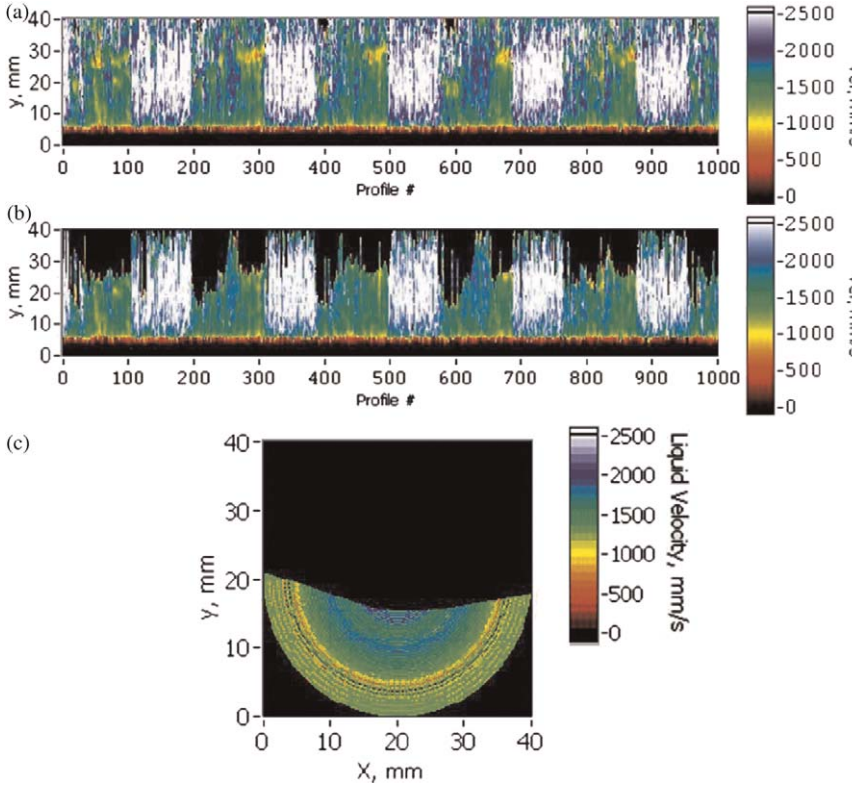

Figure 16 $Q_a = 6.2\,m^3/h$, $\alpha = 30\%$: (a) raw velocity values, (b) liquid velocity values after gas–liquid interface is detected, and (c) flow map, velocity profile # 221 (see Plate 3 in Color Plate Section at the end of this book).

Figure 16a shows the raw data of the test of $Q_a = 6.2\,m^3/h$ and $\alpha = 30\%$; the superficial liquid and gas velocities are 1.3 and 0.6 m/s, respectively. The flow condition is of the slug type, although it is close to the boundary between elongated bubble and slug flow regimes, according to the flow map developed by Govier and Omer in 1962 (in Govier and Aziz, 1972). In Figure 16a, regions of high liquid velocity (light color) and lower velocity (dark green) can be observed; the gas–liquid interface is difficult to infer from this image. After processing the echo intensity information, the gas–liquid interface is clearly revealed, as shown in Figure 16b; the interface can be found below the middle of the pipe at this void fraction. Even though the flow is of the slug type, the flow displays some features appropriate to the slug flow type. Namely, the flow exhibits large and deformed bubbles; and these bubbles fill a large part of the cross-sectional area of the pipe. The layer of liquid below the bubbles shows a slower velocity than the liquid slug does; however,

the liquid slug does not fill the entire cross-section of the pipe and small bubbles can be observed in the liquid slugs. These are small dispersed bubbles trailing the larger bubbles. The small bubbles may not ride at the top of the pipe; however, the lower extent of the distribution of these bubbles appears to be the gas–liquid interface.

Figure 16c is a sample flow map of the liquid velocity profile #221. The gas phase occupies more than 50% of the cross-sectional area of the pipe, and it is not symmetrically distributed above the liquid phase. Figure 16c also shows a higher liquid velocity near the center of the pipe that decreases radially. The lighter (yellow) lines in the lower part of the pipe and near the wall correspond to the liquid velocity values obtained from the power law equation; the darker lines (dark gray) above the power law equation values correspond to the near field effect of the transducer.

4. SUMMARY

The results presented show the gas–liquid interface can be detected by two different methods. First, we can detect changes in the velocity gradient near the interface. In this method, only velocity information of the liquid is needed; however, this method is restricted to low gas void fractions and bubbles larger than 10λ. The main motivation for applying this technique is in the development of a UVP-based sensor to reduce frictional drag. This sensor can be incorporated into ships or pipelines. Our results are part of an intermediate step crucial in the development of such a device.

Second, a peak-intensity ultrasound echo can be used to detect the gas–liquid interface, but in this case the aim is the development of a flow meter capable of estimating the ratio of component phases accurately and in real time. Our results are promising for the estimation of the liquid flow rate of gas–liquid two-phase flow; further research will produce valuable data that will allow the estimation of flow rates for the two phases simultaneously. The results presented here show the liquid flow rate estimated by the peak echo intensity method can provide an accurate estimate of the actual liquid flow rate. This method can be applied to pure liquid as well as to a two-phase flow where the void fraction is as high as 50%. The flows tested are of the stratified, elongated bubble, and slug flow types. Other types of flow such as wave flow and dispersive flow were not tested; the present experimental setup does not provide the gas and liquid flow rates needed to achieve such flows.

The expected average and standard deviations between the actual liquid flow rate and the estimated liquid flow rate are -1.9% and 5.1%, respectively, in the range $0.6 \leq Q_a \leq 7.2\,\mathrm{m}^3/\mathrm{h}$. The large standard deviation is due to the tests of $Q_a = 0.6\,\mathrm{m}^3/\mathrm{h}$. Small differences between the estimated liquid flow rate and the actual liquid flow rate represent a large δ_e value.

In the range $1.8 \leq Q_a \leq 7.2\,\mathrm{m}^3/\mathrm{h}$, the expected average and standard deviations between the actual liquid flow rate and the estimated liquid flow rate are −2.6% and 2.6%. Although the average value increases, the standard deviation value decreases by 42%.

This method for locating the position of the gas–liquid interface can be applied in parametric studies; the gas–liquid interface is an important parameter for predicting the behavior of these types of two-phase flows. Accurate gas–liquid interface detection may help improve existing two-phase flow models; this may lead to the development of more reliable and efficient equipment for handling two-phase flow.

LIST OF SYMBOLS

A_{wet}	portion of the cross-sectional area of the pipe occupied by the liquid phase (m^2)
$B(x,y)$	binary matrix
c	speed of sound (m/s)
$C_c(i)$	correlation coefficient
C_I	channel where the gas−liquid interface is located
d	bubble diameter (m)
D	pipe inner diameter (m)
E_I	raw echo intensity
f	transmitting frequency (Hz)
H	channel height (m)
$h_n(N)$	gas–liquid interface location (mm)
k	channel number
$k_{\max}$	channel number of the closest channel to the upper wall of the pipe
L	channel length (m)
N	velocity profile number
$N_{\max}$	number of velocity profiles captured
N_{UC}	cycles per ultrasonic pulse
Q_a	actual liquid flow rate (m^3/h)
Q_e	estimated liquid flow rate (m^3/h)
Q_g	gas flow rate (m^3/h)
R_e	95% confidence interval range of the δ_e values
Re_D	Reynolds number based on the superficial velocity and pipe diameter of the liquid
Re_H	Reynolds number based on the average liquid velocity and channel height
$s(x,y)$	gas–liquid interface height (mm)
t	time delay between transmitted signals (s)

u	liquid velocity distribution subtracted from mean liquid velocity of each velocity profile (m/s)
$\overline{V}$	average liquid velocity (m/s)
V_g	gas phase superficial velocity (m/s)
V_l	liquid phase superficial velocity (m/s)
$V(r,\theta)$	liquid velocity values, cylindrical coordinates (m/s)
$V(x,y)$	liquid velocity values, Cartesian coordinates (m/s)
W	channel width (m)
We	Weber number
y	vertical distance from the tip of the transducer to the gas–liquid interface (mm)

GREEK SYMBOLS

α	gas phase void fraction
δ_e	difference between the actual liquid flow rate Q_a and the estimated liquid flow rate Q_e
φ	thickness of the standing wave (mm)
λ	ultrasound wavelength (m)
$\mu_{\delta e}$	average of δ_e values
ν	kinematic viscosity of the liquid
θ	angle of the ultrasonic transducer with respect to the flow (degrees)
ρ	liquid-phase density (kg/m^3)
σ	surface tension of the liquid (N/m)
$\sigma_{\delta e}$	standard deviation of δ_e values
$\sigma_{j,k}$	covariance of the gas–liquid interface height for series j and k
σ_j	standard deviation of the gas–liquid interface height for series j (transducer 2); series j consists of N–i elements, where $j = 2$
σ_k	standard deviation of the gas–liquid interface height for series k (transducers 1 and 3); series k consists of N–i elements, where $k = 1, 3$

ACKNOWLEDGMENTS

The authors wish to thank the New Energy Development Organization of Japan for their support of this study, project number 05A45002d. The technical support of Mr. T. Sampo and support of the members of the *Laboratory for Flow Control*, Hokkaido University, is also appreciated. Professor Yasunori Watanabe of the Civil Engineering Department, Hokkaido University contributed to the research work concerning the third UVP–DUO system; his assistance in conducting this research is highly appreciated.

REFERENCES

Brennen, C. E., "Fundamentals of Multiphase Flow". Cambridge University Press, New York, NY (2005).

Cha, J. E., Ahn, Y. C., and Kim, M. H. *Flow Meas. Instrum.* **12**, 329–339 (2002).

Cook, M., and Behnia, M. *Chem. Eng. Sci.* **55**, 2009–2018 (2000).

Duckler, A. E., and Hubbard, M. *Ind. Eng. Chem. Fundam.* **14**, 337–347 (1975).

Fossa, M., Guglielmini, G., and Marchitto, A. *Flow Meas. Instrum.* **14**, 161–168 (2003).

Govier, G. H., and Aziz, K., "The flow of complex mixtures in pipes". R. E. Krieger Publishing Co., Malabar, Florida (1972).

Kitagawa, A., Hishida, K., and Kodama, Y. *Exp. Fluids* **38**, 466–475 (2005).

Kreyszig, E., "Advanced Engineering Mathematics". Wiley, New York (1999).

Lhermitte, R. *Science* **182**, 258–262 (1973).

Manneville, S., Becu, L., Grodin, P., and Colin, A. *Colloids Surf. A* **270–271**, 195–204 (2005).

Manneville, S., Sandrin, L., and Fink, M. *Phys. Fluids* **13**, 1683–1690 (2001).

Melling, A. *Meas. Sci. Technol.* **8**, 1406–1416 (1997).

Met-Flow., "UVP Monitor User's Guide". Lausanne, Switzerland (2002).

Munson, B. R., Young, D. F., and Okiishi, T. H., "Fundamentals of Fluid Mechanics". Wiley (1990).

Murai, Y., Inaba, K., Takeda, Y., and Yamamoto, F. *Flow Meas. Instrum.* **18**, 223–229 (2007).

Murai, Y., Oiwa, H., Sasaki, T., Kondou, K., Yoshikawa, S., and Yamamoto, F. *Meas. Sci. Technol.* **16**, 1459–1468 (2005).

Murakawa, H., Kikura, H., and Aritomi, M. *J. Nucl. Sci. Technol.* **40**, 644–654 (2003).

Murakawa, H., Kikura, H., and Aritomi, M. *Exp. Therm. Fluid Sci.* **29**, 843–850 (2004).

Oddie, G., and Pearson, J. R. A. *Annu. Rev. Fluid Mech.* **36**, 149–172 (2004).

Pinkel, R. *J. Phys. Oceanogr.* **9**, 675–686 (1979).

Sandrin, L., Catheline, S., Tanter, M., Hennequin, X., and Fink, M. *Ultrason. Imaging* **21**, 259–272 (1999).

Sandrin, L., Manneville, S., and Fink, M. *Appl. Phys. Lett.* **78**, 1155–1157 (2001).

Satomura, S. *J. Acoust. Soc. Am.* **29**, 1181–1185 (1957).

Shemer, L. *Int. J. Heat Fluid Flow* **24**, 334–344 (2003).

Suzuki, Y., Nakagawa, M., Aritomi, M., Murakawa, H., Kikura, H., and Mori, M. *Exp. Therm. Fluid Sci.* **26**, 221–227 (2002).

Taitel, Y., and Barnea, D. *Chem. Eng. Sci.* **45**, 1199–1206 (1990).

Takeda, Y. *Int. J. Heat Fluid Flow* **7**, 313–318 (1986).

Tavoularis, S., "Measurement in Fluid Mechanics". Cambridge University Press, New York (2005).

Wada, S., Kikura, H., and Aritomi, M. *Flow Meas. Inst.* **17**, 207–224 (2006).

Wild, J. J., and Reid, J. M. *J. Acoust. Soc. Am.* **25**, 270–280 (1953).

Yang W. J., "Computer-Assisted Flow Visualization". CRC Press, Inc., Boca Raton, Florida (1994).